Aeroacoustic impact of heat exchanger installation in an industrial engine cooling module

Applied Acoustics 245 (2026) 111175

Contents lists available at ScienceDirect

Applied Acoustics

journal homepage: www.elsevier.com/locate/apacoust

Aeroacoustic impact of heat exchanger installation in an industrial engine cooling module

Francesco Bellelli [a,*], Renzo Arina [a], Stéphane Moreau [b], Francesco Avallone [a]

[a] Department of Mechanical and Aerospace Engineering, Politecnico di Torino, Torino, 10129, Italy
[b] Department of Mechanical Engineering, Université de Sherbrooke, Sherbrooke, Québec, Canada

HIGHLIGHTS

- Assessment of heat-exchanger installation effects on fan aeroacoustics using high-fidelity lattice-Boltzmann simulations.
- Comparison of four installations to isolate heat-exchanger core, frame, and gaps sealing effects on noise generation.
- The porous medium modeling of the heat exchanger core alters inflow uniformity and enhances tonal noise.
- Small casing-heat exchanger gaps cause measurable changes in recirculation and acoustic signatures.
- Casing-induced inflow distortions are the key drivers of subharmonic humps and low-frequency broadband noise.

ARTICLE INFO

Keywords:
Engine cooling fan
Heat exchanger
Noise generation mechanism
Far-field noise
Interaction
Installation

ABSTRACT

Engine cooling fan noise becomes even more difficult to predict when considering the presence of the heat exchanger upstream. This paper investigates the impact of different heat exchanger installations on the noise sources of an industrial engine cooling fan using high-fidelity lattice-Boltzmann simulations. The heat exchanger is simulated using an equivalent porous medium upstream of the fan. Four configurations are analyzed at free discharge: full cooling module (i) without and (ii) with a gap between the heat exchanger and its casing, (iii) Fan + Frame, and (iv) Fan. For the sake of comparison, configurations (iii) and (iv) are simulated by imposing a pressure difference that matches the one across the heat exchanger, to ensure that the same operating point is maintained. Results show negligible differences in the overall aerodynamic performance since the same average pressure rise is achieved. The presence of the porous medium affects the spatial distribution of the pressure field upstream of the fan, thus causing a higher tonal content compared to the configurations (iii) and (iv). Further subharmonic humps are caused by the interaction of the blades with vortex structures generated by flow separation at the tip and the casing's support structures. The presence of a geometry transition from square to round in the casing causes inflow distortions, increasing low-frequency broadband noise.

1. Introduction

Engine cooling fans are essential components of cars, providing the necessary airflow to dissipate heat generated during operation. With the increasing demand for electric vehicles, the need for high-performance cooling systems has intensified, particularly to manage heat during fast charging cycles. Since electric motors are replacing thermal engines, the relevance of noise emissions from cooling fans has rapidly gained importance. Therefore, identification [1,2] and reduction [3,4] of noise sources have already become critical in the design phase, on the same level as aerodynamic efficiency.

Several noise sources are present in engine cooling fans; they can be classified as self-noise, loading noise, and thickness noise. Their relevance depends on the operating conditions [5], the geometry of the blades [6], and their installation within the cooling module [7], the presence of stator vanes [8], and even the testing environment [9]. The main source of noise for cooling fans is typically unsteady loading noise [10], resulting from the interaction of the blades with an unsteady or inhomogeneous inflow. This results in an increase in tonal noise, broadband noise [11], or the appearance of sub-harmonic humps [12].

Fans are usually paired with heat exchangers. The latter are typically composed of a solid frame, in which a coolant core is embedded,

* Corresponding author.
Email address: francesco.bellelli@polito.it (F. Bellelli).

https://doi.org/10.1016/j.apacoust.2025.111175
Received 25 March 2025; Received in revised form 19 November 2025; Accepted 25 November 2025
Available online 7 December 2025

and where several thin tubes allow the coolant fluid to flow and refrigerate. Moreover, it is not uncommon for the fan to be joined to the heat exchanger through a casing or shroud. This is the case when the system needs to be experimentally tested both aerodynamically and acoustically. This further complicates the cooling module's aerodynamic and acoustic performance.

For example, Sortor [13] demonstrated that aerodynamic efficiency and/or acoustic emissions are generally influenced by the non-uniform pressure field induced by the heat exchanger upstream, by the air leakage between the fan shroud and the heat exchanger, and by the axial spacing between the fan and the heat exchanger core. This makes the direct comparison between fans coupled with different heat exchangers difficult. Czwielong et al. [14] showed that varying the axial spacing between the fan and the heat exchanger strongly alters the tonal noise at the Blade Passing Frequency (BPF = $B\Omega$, where B is the number of blades and Ω the fan rotational frequency in Hz) and harmonics. Moreover, they found that a decrease in the diameter of the coolant tubes reduces the broadband noise content. However, this is limited to configurations in which the diameter of the coolant tubes is still larger than the fan-heat exchanger axial spacing. They also showed that the shape of the casing causes tonal noise, thus highlighting the noise reduction benefits of circular casing shapes compared to rectangular or squared ones, due to a smoother casing-to-fan shape transition in the circular shape configuration. Zarri et al. [15] observed that densely packed coolant tubes disrupt the turbulent eddies and increase the turbulence non-homogeneity, whereas the presence of an upstream casing induces anisotropy in the turbulent field.

From an application standpoint, Amoiridis et al. [2] demonstrated that sealing the axial gap between the heat exchanger and the casing has a negligible influence on aerodynamic performance, if the gaps are sufficiently small. However, the presence of these gaps can affect the recirculation patterns within the casing, thus impacting the acoustic emissions of the fan. This aspect has not been investigated in detail in the scientific literature. Collectively, these results highlight that even small design variations in the heat exchanger or casing geometry have a significant acoustic impact. Since it is experimentally challenging to visualize the flow field for these complex systems, the experimental quantitative description of how the noise generation mechanisms are affected by these installation effects has not been fully described yet.

From the numerical perspective, Piellard et al. [16] and Lallier-Daniels et al. [7] showed the potential of high-fidelity lattice-Boltzmann simulations to identify the flow features responsible for the noise generation on cooling modules. As a matter of fact, Zhang et al. [17] stressed the importance of including the relevant elements of the heat exchanger in order to accurately predict the far-field noise. Tebib et al. [18] showed that modeling the heat exchanger as a porous medium is sufficient to accurately predict both the aerodynamic performance and the far-field noise. It was concluded that it is not necessary to explicitly simulate the geometry of the heat exchanger.

Previous studies did not describe in detail how the noise generation mechanisms are affected by a non-uniform pressure rise upstream of the fan, caused by the presence of the heat exchanger, and how these are altered by different installations. This is of essential importance, as pointed out by Czwielong et al. [19], who stated that aeroacoustic optimization of the cooling module must be a joint optimization of the heat exchanger and fan.

In this paper, we aim to explain how the installation of a heat exchanger can affect far-field noise by looking at several aspects. First, the impact of the presence of gaps between the heat exchanger and its casing is assessed by analyzing the cooling module (i) in the absence and (ii) in the presence of these gaps. Moreover, the impact of a non-uniform pressure rise, as it occurs across a heat exchanger, is compared against a uniform pressure rise that can be realized by imposing upstream pressure conditions. For this purpose, a configuration without a heat exchanger core is investigated (iii). Finally, the relevance of the heat exchanger frame is assessed by defining a configuration in which only the fan is present (iv). The latter two configurations are simulated by imposing a pressure rise that matches the one across the heat exchanger so that the same operating point is maintained. For the purposes of this study, scale-resolved high-fidelity numerical simulations are carried out with the lattice-Boltzmann method (LBM).

The results and findings presented in this paper are an extension of the conference paper in Ref. [20]. In this paper, the impact of the gap sealing and additional analyses to describe the dominant physical mechanisms are reported. In more detail, the impact of the unsteady flow features on non-harmonic humps is described.

The rest of the paper is structured as follows: Section 2 describes the methodology used to numerically calculate aerodynamic and acoustic fields, Section 3 briefly summarizes the experimental setup used to validate the numerical calculations, which are presented in detail in Section 4. The grid convergence study and the validation of the numerical simulations against the experiments are discussed in Section 5. Section 6 discusses the obtained results, while the main conclusions are outlined in Section 7.

2. Methodology

The flow field is computed using the commercial software 3DS PowerFLOW version 6, based on the LBM [21]. A more detailed description of the method and its aeroacoustic applications can be found in [22,23]. The LBM approach is extensively used for aeroacoustic studies of low-speed fans for automotive applications [24–26].

The governing equation is the continuous Boltzmann equation:

$$\frac{\partial f}{\partial t} + c\frac{\partial f}{\partial t} + \frac{F}{m_f}\frac{\partial f}{\partial c} = C, \tag{1}$$

where $f(\vec{x}, \vec{c}, t)$ is the particle distribution function, i.e., the probability that at time t and position $\vec{x}$ a particle has a velocity $\vec{c}$. F is the external force, m_f is the molecular weight of the fluid, and C is the collision operator, which models the variations in the distribution function caused by collisions between two particles. The collisions are elastic; therefore, mass, momentum, and kinetic energy are conserved. The Bhatnagar, Gross, Krook (BGK) collision operator [27] is adopted

$$C = -\frac{1}{\tau}(f - f^{eq}), \tag{2}$$

where τ is the relaxation time and f^{eq} is the Maxwell-Boltzmann equilibrium distribution function. The Navier-Stokes equations can be recovered from Eq. (1) for low Mach numbers by means of a Chapman-Enskog expansion [28].

Eq. (1) is discretized in space by dividing the computational domain into cubic lattices, called voxels, where particles can move only in a fixed number of directions. In its low Mach number solver version, adopted in this work, the model with 19 discrete velocity directions in three dimensions [29] is used. To simulate the rotating components, a sliding mesh approach is used [30].

To properly capture the largest turbulent structures and reduce the computational cost, compared to resolving all turbulence scales, a Very Large Eddy Simulation (VLES) approach is employed by modifying the relaxation time to include the contribution of the spatial filtering as

$$\tau_{eff} = \tau + \tau_{turb}. \tag{3}$$

The subgrid model is derived from the renormalization group $k-\epsilon$ transport equations (RNG $k-\epsilon$) [31]. The pressure-gradient extended wall model (PGE-WM) [32], an extension of the generalized wall model proposed by Launder and Spalding [33], is used to further reduce the computational cost.

3. Geometry and experimental setup

The fan consists of a $D = 465$ mm diameter rotor with $B = 11$ unevenly spaced blades connected to a ring, a hub, a driving electrical

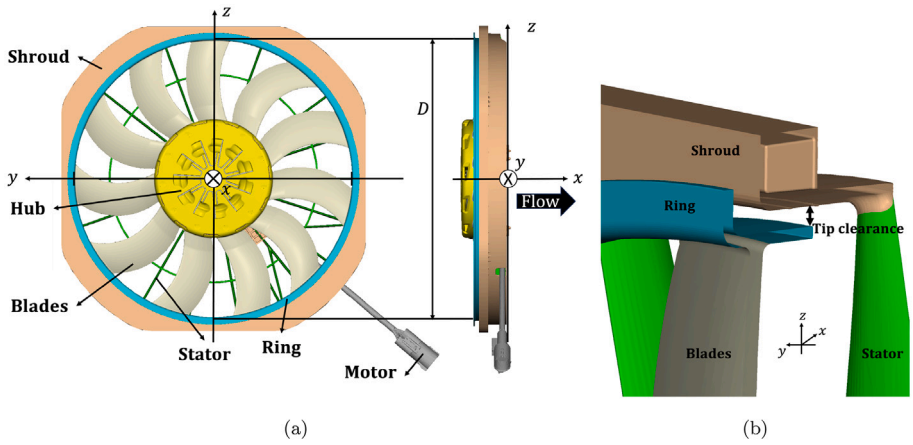

Fig. 1. Tested automotive fan. The main parts of the fan module are shown with different colors. (a): Cooling fan. (b): Tip clearance detail.

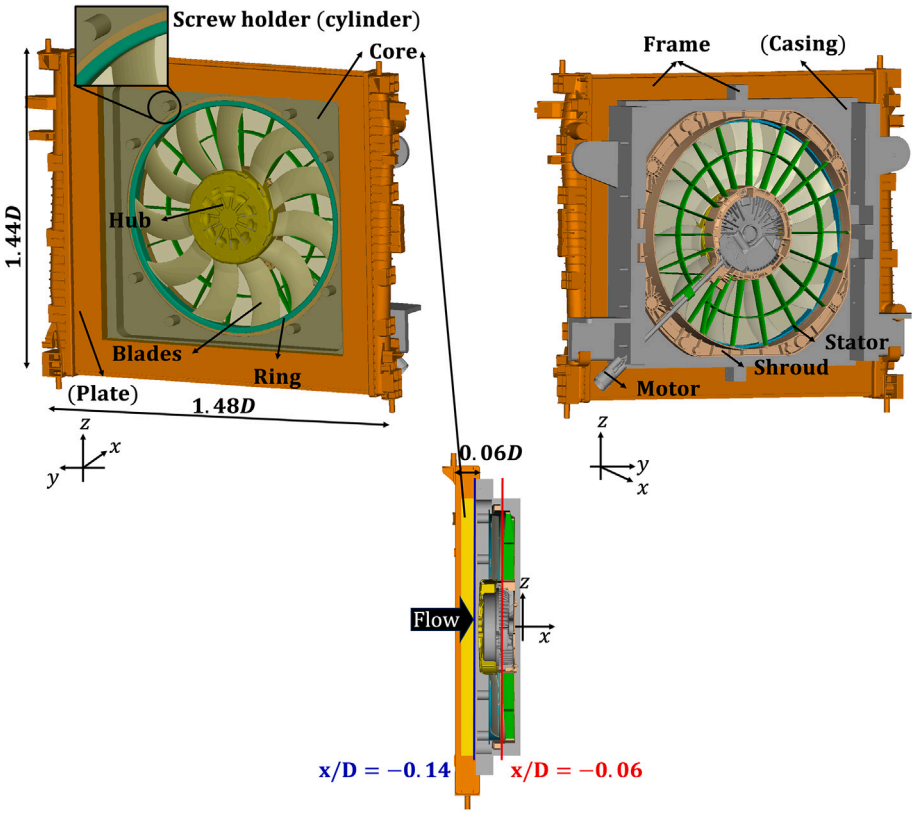

Fig. 2. Tested cooling module. The heat exchanger is shown in orange (solid plate) and yellow (core, simulated as porous medium) while the square casing is shown in grey. The upstream ($x/D = -0.14$) and downstream ($x/D = -0.06$) planes, where the averaged flow field will be shown, are highlighted respectively in red and blue.

motor, $N_v = 20$ unevenly spaced stator vanes, and a shroud, as shown in Fig. 1(a). The fan tip clearance is equal to $0.009D$ and is shown in Fig. 1(b).

The heat exchanger consists of a plate of $1.48D \times 1.44D \times 0.06D$ placed $0.02D$ upstream of the fan hub and of a square casing that is joined to the fan shroud through 8 screws, covered by upstream protruding cylinders, as shown in Fig. 2. The solid plate in orange of the heat exchanger joined with the square casing in grey will be referred to as “Frame” in the rest of the paper. The core part of the heat exchanger is shown in yellow in Fig. 2. Further details on how it is modeled are given in Section 4.

Reference experimental data, acquired and provided by the manufacturer, are used to validate the numerical simulations. Volume flow rate and torque are measured in an aerodynamic facility, while acoustic measurements are performed in a semi-anechoic room. During both measurements, the axial gaps between the heat exchanger and the square casing are sealed. The aerodynamic performances are described using dimensionless parameters.

Flow rate and torque measurements are carried out along the full operating range for both the fan alone and the complete cooling module, while acoustic measurements are carried out only at free discharge conditions for the complete cooling module, corresponding to a load coefficient equal to

$$\psi = \frac{\Delta p}{\frac{1}{2}\rho v_{tip}^2} = 0, \tag{4}$$

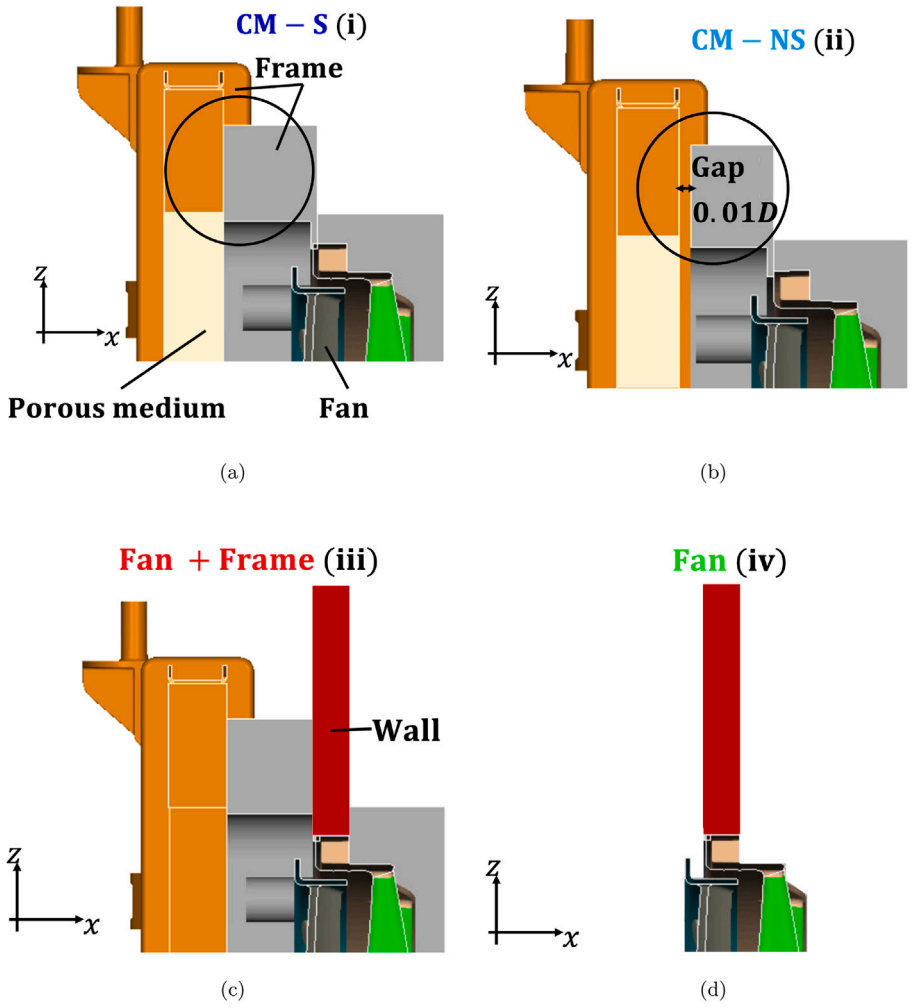

Fig. 3. Sketch of the four simulated configurations.

where $\Delta p = p_{amb} - p$ is the fan pressure rise, ρ is the air density, $v_{tip} = \Omega R_{tip}$ is the tip velocity, and $R_{tip} = D/2$ is the fan tip radius. The flow coefficient is equal to

$$\varphi = \frac{\dot{V}}{\pi \left(R_{tip}^2 - R_{hub}^2 \right) v_{tip}} = 0.13, \tag{5}$$

where $\dot{V}$ is the volume flow rate through the fan and R_{hub} is the hub radius. These values have been obtained considering a fan rotational speed $\Omega = 3048$ RPM.

The aerodynamic facility is certified according to the AMCA 210-99 standard and is described in a previous work by the authors [9]. The pressure rise is set by lowering the pressure in the upstream chamber and is recorded through a pressure sensor. The flow rate is measured with a standardized volumetric flow meter, while the torque is measured with a torque meter. These quantities are recorded for a 3 s interval, during which it is checked that the pressure rise lies within a 1 % band of the desired value. The driving electric motor is supplied with varying shaft power to ensure that the fan spins at a constant rotational speed.

The acoustic facility consists of a semi-anechoic room $10.75D \times 10.75D \times 6.45D$, with the floor at a distance of $z/D = 3.23$ from the fan center, placed in the center of the room. A $1/2\,\varepsilon$ PCB Piezotronics far-field microphone is placed at $x/D = -2.15$ upstream of the fan, aligned with the fan rotational axis. The sound pressure signal is acquired for 30 s at a sampling frequency of 25.6 kHz, and its spectral content is computed through the Welch averaging algorithm [34] with 1280 Hamming windows (each window covers 5 fan revolutions) and 50 % of overlap, resulting in a frequency resolution of 11.8 Hz so that both numerical and experimental signals have the same characteristics and a fair comparison can be made.

4. Numerical setup

The cooling fan with and without the heat exchanger is simulated. The geometries adopted are the same as those tested experimentally (Figs. 1(a) and 2).

Fig. 3 shows the four different simulated configurations to assess the heat exchanger installation effects. Firstly, two different installations of the full Cooling Module (CM) have been simulated: in the (i) first one (Fig. 3a), the axial clearance between the casing and the heat exchanger has been sealed as done in the experiments (CM-S), while in the (ii) second one (Fig. 3b) the clearance has been kept equal to $0.01\,D$ on all four sides of the interface (CM-NS). This value is an average of what has been experimentally measured along the full extent of the sides of the casing, caused by elastic deformations. Moreover, two additional configurations are analyzed to assess the effects of the porous medium and the frame: in the (iii) third configuration (Fig. 3c), the porous medium has been removed (Fan + Frame), and in the (iv) fourth configuration (Fig. 3d), both the porous medium and the frame have been removed (Fan).

The computational domain used to simulate all the configurations is shown in Fig. 4. A large fluid domain of $135D \times 135D \times 135D$ is built enclosing the semi-anechoic room. The room walls, of the same size as

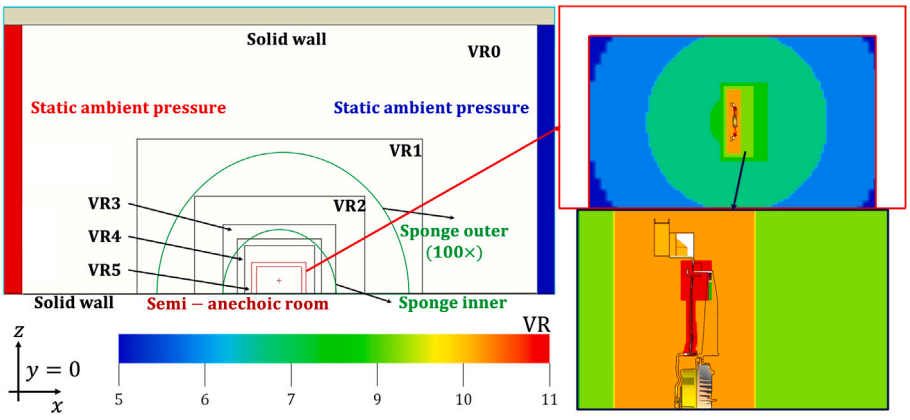

Fig. 4. Sketch of the computational domain for the CM-S in the plane at $y/D = 0$.

the experimental ones, are modeled as an equivalent porous medium with viscous resistance equal to 50000 1/s along the three Cartesian directions. The floor is modeled as a solid reflective wall to emulate the experimental facility. A discretization strategy based on 11 Variable Resolution (VR) regions is adopted. The regions with maximum resolution are set around the rotating blades and near the tip gap region, where, for the most refined case, there are 11 voxels in the tip clearance. The resolution in the tip gap region is similar to the one adopted by Avallone et al. [35]. The voxel size between one VR region and the adjacent one is doubled. In the VR3 region, a sponge region is defined by an artificial change in viscosity by a factor of 100, with an exponential function between the inner and outer regions, as outlined in Fig. 4. Both the increase in voxel size and the sponge region are used to mitigate reflections of acoustic waves at the domain boundaries. Both inlet and outlet boundaries have a static ambient pressure boundary condition. The ceiling of the simulation domain is modeled as a solid reflecting wall.

In the Cooling Module configurations, the heat exchanger is modeled as an equivalent porous fluid [16]. The heat exchanger characteristic curve has been measured by the manufacturer in the same aerodynamic testing facility described in Section 3 and modeled through Darcy's law [36] in terms of pressure drop Δp across the heat exchanger core:

$$\frac{1}{\rho}\frac{\Delta p}{\Delta x} = Iu^2 + Vu, \tag{6}$$

where u is the axial velocity component. The viscous resistance coefficient V is equal to 413 1/s while the inertial resistance coefficient I is equal to 116 $1/m$. The axial width of the heat exchanger core Δx is equal to $0.06D$. The V and I coefficients have been obtained by fitting the experimentally measured heat exchanger characteristic curve as explained in [18].

In the Fan + Frame and Fan configurations, as the porous medium is removed, upstream of the fan, pressure is imposed to match the global pressure rise of the porous medium under the same operating conditions. To achieve this, a thin and acoustically absorbing wall is added to the computational domain [9]. The pressure rise is imposed by initializing the flow on the suction side of the domain with a static pressure equal to the difference between the ambient pressure and the pressure rise. The inlet boundary condition is adjusted accordingly, similar to what was done in a previous work [9].

The experimental aerodynamic characteristic curves of the complete cooling module (CM), the fan alone, and the heat exchanger alone (PM) are shown in Fig. 5. To calculate the matching pressure rise, it is assumed that the pressure drop given by the heat exchanger is completely counterbalanced by the fan pressure rise. Therefore, the matching pressure rise is calculated as the pressure rise that the fan alone (red curve)

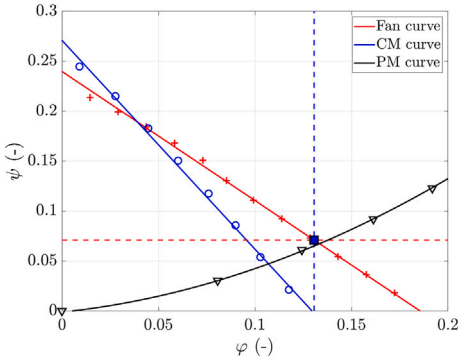

Fig. 5. Experimental aerodynamic performance curves of fan alone (Fan), complete cooling module (CM), and heat exchanger alone (PM). The markers are some of the experimental values, while the solid lines are first-order interpolation for the cooling module and fan curves, and second-order interpolation for the porous medium curve on all the recorded points.

would achieve at a flow rate that corresponds to the free discharge condition ($\psi = 0$) of the complete module (blue curve), as the only pressure drop would be caused by the heat exchanger. In this work, the flow rate at free discharge operating condition for the complete cooling module is $\varphi = 0.13$; therefore, the matching pressure rise is $\psi = 0.071$. It is worth noting that the porous medium characteristic (black curve) in Fig. 5 exhibits a good match with the calculated pressure rise at $\varphi = 0.13$ since there is almost no installation effect on the cooling module, thus giving confidence that the adopted methodology is reasonably accurate.

A physical time of 60 revolutions is simulated for every case, and data are saved during the last 10 revolutions. Three simulations have been performed at three different resolutions (res) equal to 300 vox/D, 600 vox/D, and 1200 vox/D in the finest VR region. Each simulation is initialized with the last snapshot of the previous resolution so that the flow can properly develop without increasing the computational cost. Moreover, a grid convergence study is performed, as will be shown in Section 5.

Pressure and velocity are sampled at 48,000 Hz on two perpendicular planes located at $y/D = 0$ and $z/D = 0$, respectively. Three planes parallel to the fan are sampled at 3000 Hz; they are located at $x/D = -0.14$, $x/D = -0.06$, and $x/D = 0$, and are used to compute phase-locked flow fields. The three locations correspond respectively to the rotating ring upstream boundary, the rotor–stator interstage, and the stator vane trailing edge. Moreover, a small volume around the fan module is sampled at a frequency of 755 Hz and used to generate instantaneous flow field visualizations. All the solid surfaces of the cooling module are sampled

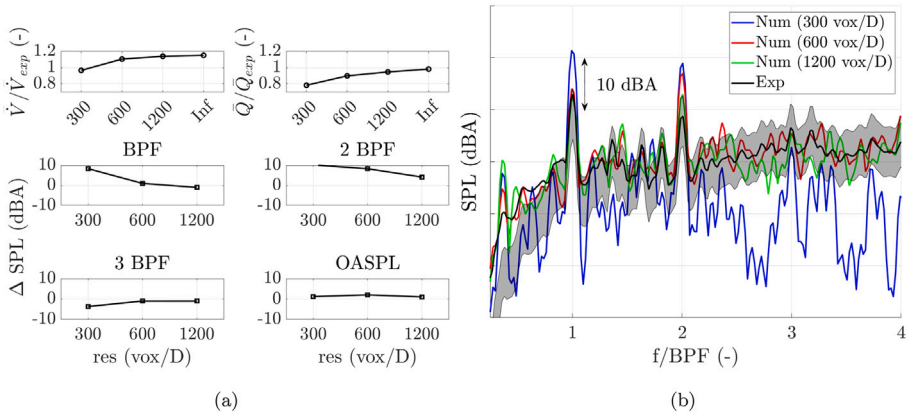

Fig. 6. Grid independence study for the CM-S. (a): Integral aerodynamic and acoustic quantities made dimensionless with or referred to the corresponding experimental values. The volume flow rate shows the following convergence indices: $GCI^{\dot{V}}_{2,3} = 2\,\%$, $GCI^{\dot{V}}_{1,2} = 0.2\,\%$, $R_{\dot{V}} = 1$. The aerodynamic torque shows the following convergence indices: $GCI^{Q}_{2,3} = 9.1\,\%$, $GCI^{Q}_{1,2} = 2.3\,\%$, $R_Q = 1$. (b): Sound Pressure Level in dBA obtained at $2.15D$ along the fan axis upstream. The solid black line represents the averaged signal on the entire sampling period, while the grey shade represents the interval of variation in SPL for windows of 10 revolutions in the experimental signal.

at a frequency of 48,000 Hz and used to compute band-pass filtered maps of wall pressure fluctuations.

Integral values of blade loading, torque, and mass flow rate are sampled as well. The mass flow is sampled at a frequency of 48,000 Hz in a plane located at $x = 0/D$.

Finally, a fully circular array of 360 equally spaced far-field probes, located in the plane $z/D = 0$ at a radius $\sqrt{x^2 + y^2}/D = 2.15$ far from the fan center, is used to sample directly the acoustic field from the simulations and perform directivity analyses. The spectral content of the probe signals is computed through the Welch averaging algorithm [34] with 8 Hamming windows and 50 % of overlap, resulting in a frequency resolution of 11.8 Hz.

5. Grid convergence and numerical setup validation

As a first step, a sensitivity analysis of the grid for the CM-S configuration is performed due to the availability of experimental data.

The volume flow rate through the fan and the aerodynamic torque ($\bar{Q}$) obtained from the simulations are shown in Fig. 6(a). The quantities have been made dimensionless with the corresponding experimental values (exp) and averaged over the last 10 revolutions (bar superscript). The "Inf" values are obtained through a Richardson extrapolation [37] with a refinement ratio $r = 2$ and an order of convergence $p = 2$ [38]. The corresponding values for the grid convergence index (GCI) and the ratio $R = \frac{GCI_{2,3}}{r^p GCI_{1,2}}$ are reported in the figure. The latter shows that grid convergence is reached for the finest resolution case, as the extrapolated values are sufficiently close to the finest resolution (within 2 %). The volume flow rate shows convergence, although it results in a slight overestimation of the experimental value. On the other hand, the torque is characterized by a steeper variation between resolutions and is underestimated with respect to the corresponding experimental value. The differences in torque can be attributed to the difficulty in measuring a pure aerodynamic torque, while the discrepancies in flow rate might be associated with a slightly different recirculation pattern in the casing, since the simulated physical time is different from the experimental acquisition time. These issues have been previously assessed by Moreau et al. [39]. However, results are aligned with similar cases in the literature [40], the GCI values are sufficiently small, and the ratio R is sufficiently close to $R = 1$, in accordance with what is stated by Roache [41].

Fig. 6(a) shows the SPL $= 20\log_{10}\left(\frac{p_\sigma}{2\cdot10^{-5}}\right)$, where p_σ is the pressure standard deviation, at the BPF and the first two harmonics as well as the integrated overall SPL (OASPL) $= 10\log_{10}\left(\sum_i 10^{SPL(f_i)/10}\right)$ in terms of difference against the experimental values. Also, these quantities are grid independent, and the difference with respect to the experiments is within 3 dBA. In particular, the BPF and first harmonic are overestimated, while the second harmonic is underestimated; the OASPL instead shows less dependence on the resolution. This is consistent with what was found in [2].

Table 1
Mean aerodynamic integral quantities percentage variations with respect to the CM-S configuration. For each case, the quantities have been averaged over the last 10 revolutions.

	$\Delta\bar{T}$	$\Delta\bar{\dot{V}}$	$\Delta\bar{Q}$
CM - S	0 %	0 %	0 %
CM - NS	−1.45 %	+0.43 %	−0.67 %
Fan + Frame	−12.61 %	+2.49 %	−4.96 %
Fan	−5.47 %	+0.62 %	−6.41 %

The spectrum obtained at $x/D = -2.15$ along the fan axis upstream from the direct probe, at the three resolutions, is compared against the experimental one in Fig. 6(b). The grey-shaded area represents the variability in the SPL during the complete sampling time of the experimental values ($30\,s$) for windows of 10 revolutions, i.e., the same number of revolutions sampled in the numerical simulations; this has been done because of the notable differences between the sampling period of the simulations and experiments. First, the coarse resolution ($300\,vox/D$) is seen not to be sufficient to properly capture any broadband content, while the tones up to the first BPF harmonic are overestimated; this might justify an OASPL that is not particularly different from the experiments. The medium ($600\,vox/D$) and fine ($1200\,vox/D$) resolutions are instead able to correctly predict the broadband levels and are characterized by a less prominent tonal content at BPF and harmonics. Furthermore, the finest resolution shows better agreement at higher BPF harmonics; therefore, the results in the rest of this paper are shown only for the $1200\,vox/D$ resolution, as they provide confidence that the underlying physical mechanisms are correctly captured by the simulations.

6. Results and discussion

6.1. Aerodynamic results

First of all, the impact of the different configurations on the mean integral aerodynamic performance is assessed. In Table 1, the mean

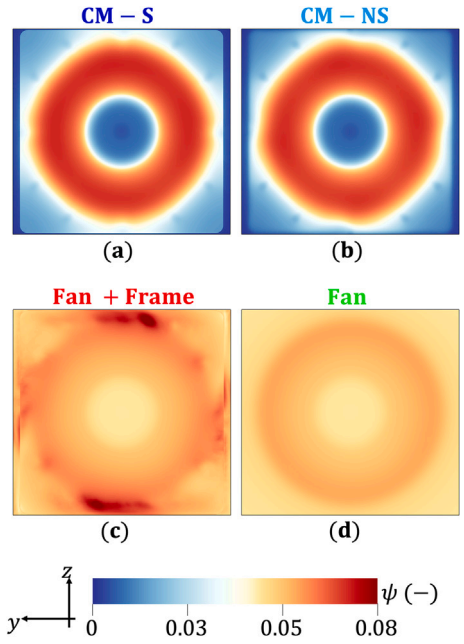

Fig. 7. Mean pressure rise with respect to the ambient pressure in a plane located at $x/D = -0.14$, upstream of the fan. (a): CM-S. (b): CM-NS. (c): Fan + Frame. (d): Fan.

thrust ($\bar{T}$), volume flow rate through the fan, and aerodynamic torque are shown as percentage variations with respect to the reference CM-S configuration. The presence of small gaps between the square casing and the heat exchanger does not affect these quantities, as the variations are within 2 %. Removing the porous medium but maintaining the global pressure rise (Fan + Frame) has a significant effect on both thrust and torque, which are reduced respectively by 14 % and 5 %, while keeping the flow rate mainly unaltered. The reason for this reduction might be due to the different inflow spatial distribution between the Fan + Frame and the full Cooling Module configurations. This leads, in the former case, to more severe flow distortions decrease the loading on the fan. For the Fan alone configuration, a negligible variation in the volume flow rate is observed. It can also be noticed that the thrust decreases only by 5 % while the torque decreases by 6 %, meaning that the Fan + Frame configuration is characterized by lower thrust and higher torque than the Fan alone configuration. This trend is explained by considering that for the Fan alone configuration, the inflow is uniform, thus leading only to a slight variation in the thrust as well as to a lower drag (i.e., lower torque). The observed discrepancies in thrust and torque are also attributed to a slight underestimate in the matching pressure rise calculation, presented in Section 4.

In Fig. 7, contour plots of pressure rise ψ for all the simulated configurations in a plane located at $x/D = -0.14$ upstream of the fan and downstream of the heat exchanger are shown. It can be noted that the gap sealing (Fig. 7b) does not particularly change the ψ pattern, showing only some differences in the tip region. Conversely, the effect of the porous medium (Fig. 7a) is evident, as it concentrates the pressure rise mainly on the fan disk, unlike the Fan + Frame (Fig. 7c) and Fan (Fig. 7d) configurations, which show a more uniform distribution of ψ. This behavior is a direct consequence of the fact that the porous medium causes a pressure rise that depends on the inflow velocity. Therefore, a higher pressure rise in the region characterized by higher inflow velocities, such as the fan disk, is found. It is also worth noting that the tip area is characterized by a lower ψ in the configurations with the porous medium (Fig. 7a and b). The square casing (Fig. 7c) is responsible for high ψ spots at the center of each side due to flow distortions caused by the square-to-round shape transition between the casing and the fan, resulting in stronger local flow acceleration in the regions with shorter fan-frame distances. Finally, the Fan alone configuration (Fig. 7d) is characterized by a highly uniform distribution of ψ, as the porous medium is removed as well as any possible source of flow recirculation and inflow distortion. These effects on the pressure rise distribution influence the velocity profiles upstream of the fan.

Figs. 8 and 9 show the azimuthally averaged velocity profiles upstream ($x/D = -0.14$) and downstream ($x/D = -0.06$) respectively. All the quantities are made dimensionless with the tip velocity v_{tip} and shown as a function of the spanwise coordinate $r = \sqrt{y^2 + z^2}$ on the blade. Firstly, the gap sealing is seen not to affect the mean velocity both upstream and downstream. Then, it can be noted that the porous medium is characterized by lower values of mean axial velocity u upstream (Fig. 8a) in the range $0.5 \leq r/R_{tip} \leq 0.95$ as a consequence of higher pressure rise, as seen in Fig. 7. On the contrary, near the hub ($r/R_{tip} \leq 0.5$), the axial velocity upstream (Fig. 8a) is higher, as the pressure rise is nearly equal to zero. Downstream (Fig. 9), the presence of the porous medium causes higher values of the tangential component v_θ (Fig. 9c) and also of the radial component (Fig. 9b) up to $r/R_{tip} \leq 0.7$. For $r/R_{tip} > 0.7$ the presence of the porous medium causes lower values of the radial component v_r instead. The axial velocity (Fig. 9a) remains unaltered, except in the region $0.9 \leq r/R_{tip} \leq 1$ in both CM configurations. Moreover, the presence of the Frame results in higher values of the radial and tangential velocity components upstream (Fig. 8b and c) for $r/R_{tip} \geq 0.9$. This might indicate the presence of higher flow recirculation in the casing when the porous medium is removed, as the pressure rise is increased.

Since the main differences are observed in the axial velocity upstream, a closer examination of this quantity is conducted in the near-tip region, within the range $0.8 \leq r/R_{tip} \leq 1.1$, upstream of the fan ($x/D = -0.14$) in Fig. 10. The CM-NS configuration exhibits a slight deviation from the CM-S case for $r/R_{tip} \geq 1.05$, which is associated with a different recirculation pattern in the casing. Moreover, the presence of the porous medium (CM-S, CM-NS) increases the axial velocity gradient, as a result of the highly non-uniform ψ compared to the configurations without the porous medium (Fan + Frame, Fan) observed in Fig. 7. In addition, the presence of the porous medium (CM-S, CM-NS) results in lower axial velocity values for $r/R_{tip} \leq 0.95$. The Fan + Frame configuration shows negligible differences compared to the CM-S and CM-NS configurations in the axial velocity in the near-tip region, up to $r/R_{tip} \approx 1.03$, while the Fan configuration reveals the presence of a small negative axial velocity region for $r/R_{tip} \geq 1.04$, suggesting the presence of flow recirculation. These changes in the inflow topology further affect the mean loading distribution on the blades.

The distribution of thrust per unit length $\bar{T}/\Delta r$ on one reference blade is shown in Fig. 11 as an averaged value over the last 10 revolutions. The plot shows that the configurations with the porous medium are characterized by higher thrust per unit length up to $r/R_{tip} \leq 0.9$ as a result of higher ψ on the fan disk. In addition, the velocity drop near the tip, seen in Fig. 10, results in lower thrust per unit length for $r/R_{tip} > 0.9$. The effects of the gap sealing are slightly visible only in the near-tip region, as a consequence of the small variations in the velocity gradient. Finally, the different flow topologies near the hub are seen to cause a hump on the thrust per unit length at $r/R_{tip} = 0.45$, due to the recirculation in the hub. It is worth mentioning that the hub presents several small slots that allow for the cooling of the driving electric motor; therefore, flow recirculation happens in those areas, especially in the presence of strong gradients.

The skin friction (τ_w) coefficient $c_f = \tau_w/(1/2\rho v_{tip}^2)$ is shown in Fig. 12 on the blades pressure side. It can be noted that all the simulated cases present flow separation on the pressure side, near the tip area, as the skin friction coefficient approaches zero. This separation is a consequence of the high flow rate at which the fan is operating, which causes the axial component of the velocity to increase the upwash angle seen by the blades. Moreover, both the configurations with the porous medium (Fig. 12a and b) are characterized by more visible regions of nearly-zero skin friction coefficient also in the hub area, which represent the trace

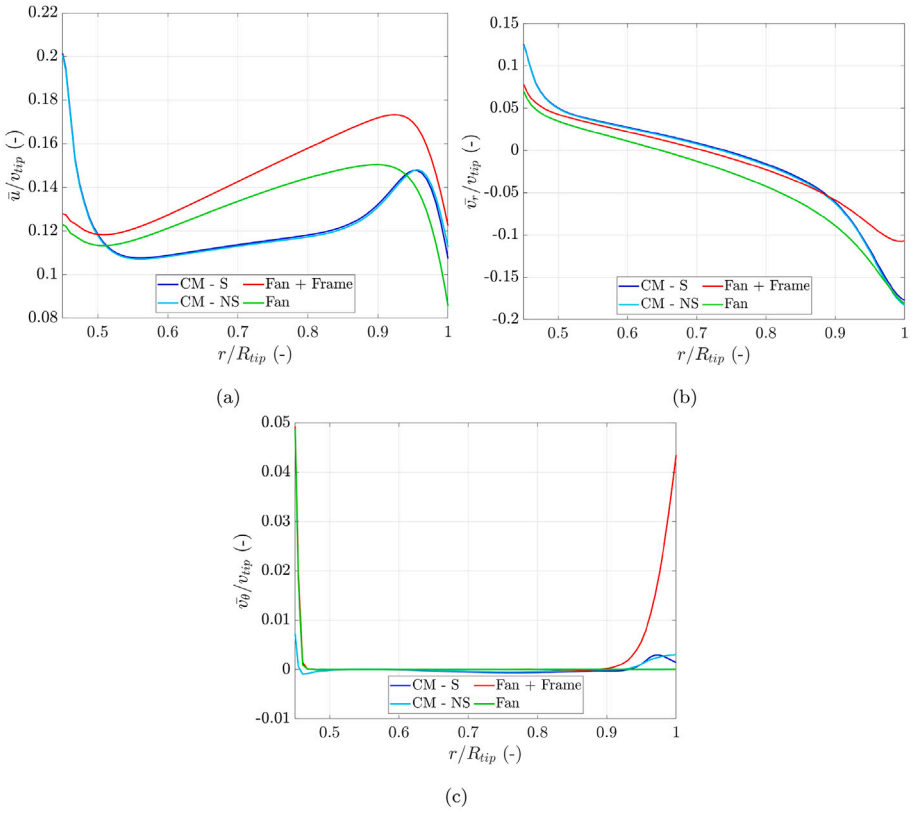

Fig. 8. Velocity profiles azimuthally averaged at $x/D = -0.14$. (a): Axial velocity component. (b): Radial velocity component. (c): Tangential velocity component.

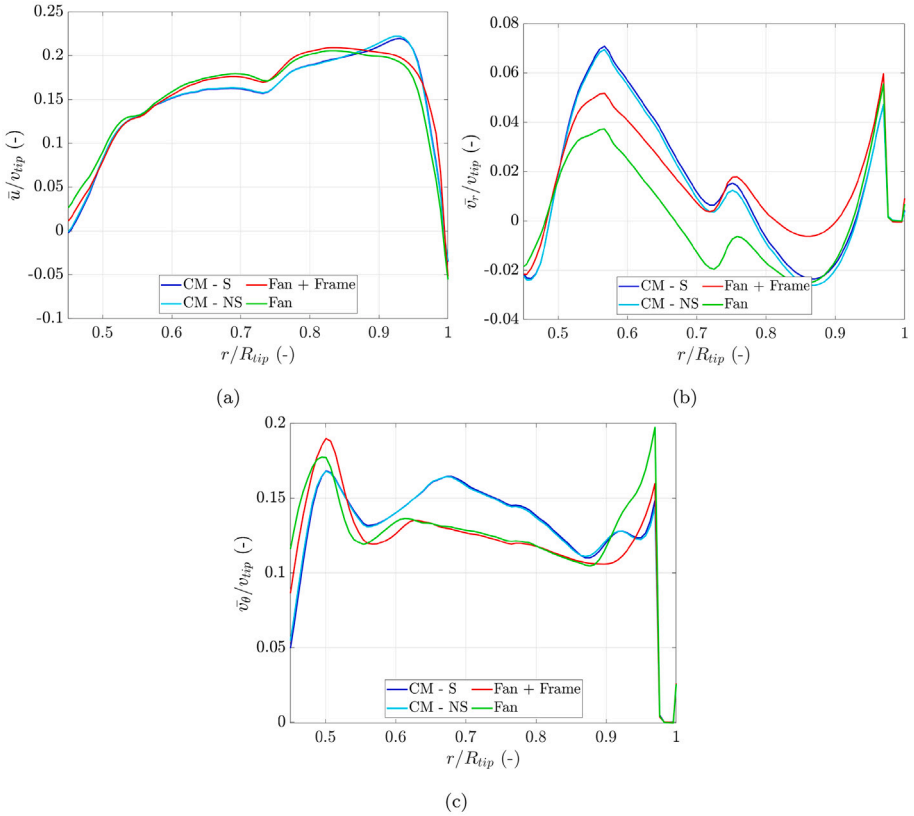

Fig. 9. Velocity profiles azimuthally averaged at $x/D = -0.06$. (a): Axial velocity component. (b): Radial velocity component. (c): Tangential velocity component.

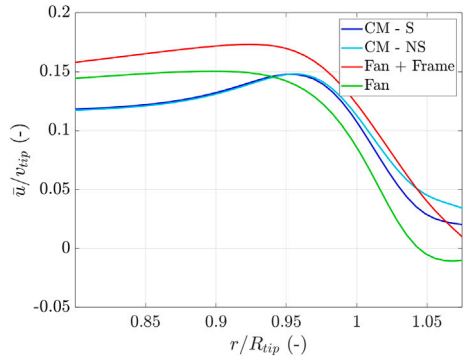

Fig. 10. Mean axial velocity in the near-tip region ($0.8 \leq r/R_{tip} \leq 1.1$), at $x/D = -0.14$, azimuthally averaged.

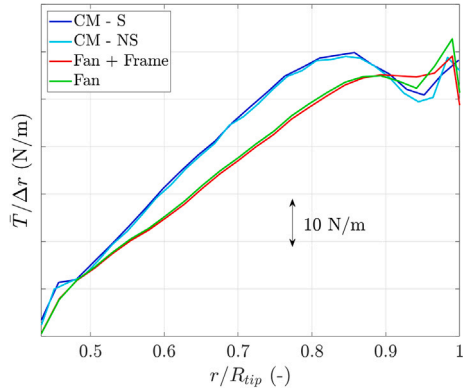

Fig. 11. Mean thrust per unit length distribution on one blade, averaged on the last 10 revolutions.

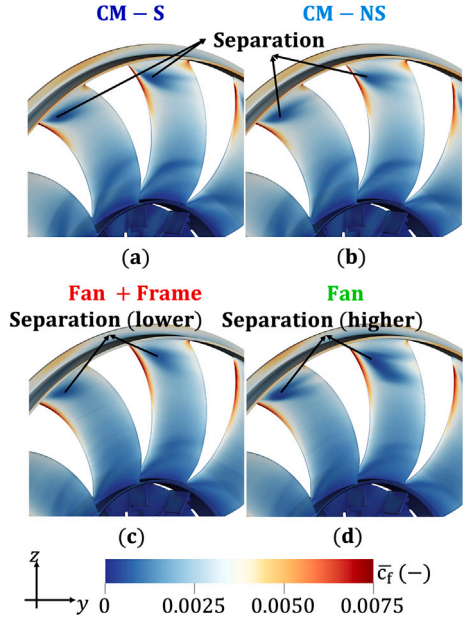

Fig. 12. Mean skin friction coefficient on the pressure side of the fan. (a): CM-S. (b): CM-NS. (c): Fan + Frame. (d): Fan.

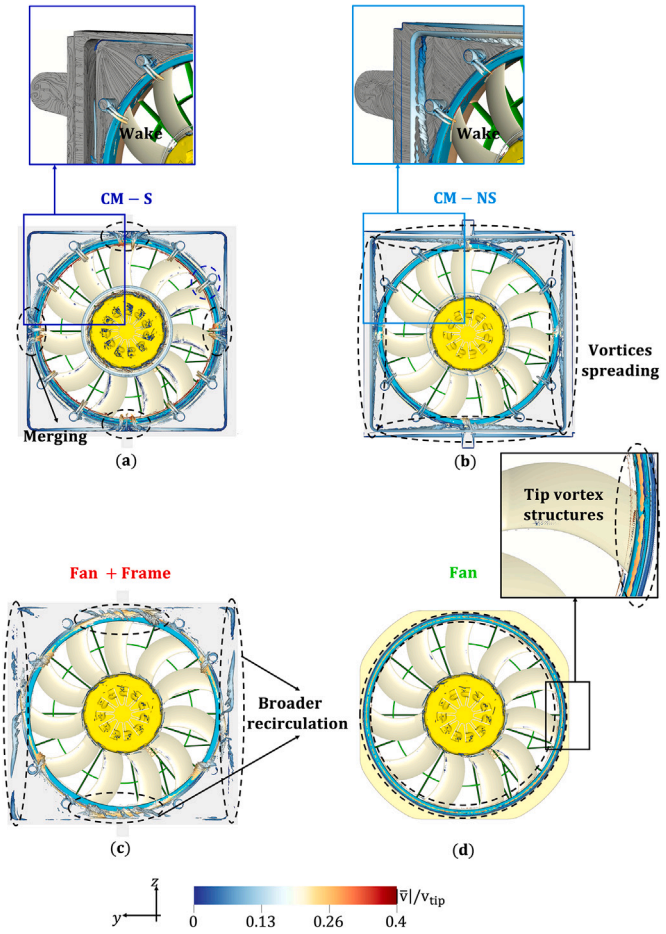

Fig. 13. Mean $\Lambda_2 = -2.5 \cdot 10^5$ 1/s iso-surfaces colored with velocity magnitude in the casing upstream. (a): CM-S. (b): CM-NS. (c): Fan + Frame. (d): Fan.

of the horseshoe vortex formed upstream of the blade. This suggests that flow recirculation is happening near the hub as well. Finally, it is seen that the Fan configuration (Fig. 12d) is characterized by a more severe separation at the tip. This might be associated with the slightly higher inflow velocity that corresponds to this configuration, as seen in Fig. 10.

The analyses above have highlighted the relevance of the flow recirculation in the casing on the mean flow topology and on the blade loading distribution. The $\Lambda_2 = -2.5 \cdot 10^5$ 1/s iso-surfaces colored with dimensionless velocity magnitude $|v|/v_{tip} = \sqrt{u^2 + v_r^2 + v_\theta^2}/v_{tip}$ are shown in Fig. 13. The quantities are shown only in the square casing area. For the Cooling Module configurations, a zoom of a quarter of the casing volume is shown with streamlines superimposed on the casing surface. First of all, one can note that the CM-S configuration (Fig. 13a) is characterized by coherent vortex structures along the four sides of the casing, which strongly merge at the center of each side. On the other hand, the CM-NS configuration (Fig. 13b) shows a more spread recirculation along the sides of the casing. This is a consequence of the flow leakage through the $0.01D$ gap between the casing and the heat exchanger solid part, which has been quantified to be approximately 5 % of the mean fan flow rate. Moreover, both the CM-S and CM-NS configurations show the presence of wakes shed by the 8 cylinders that house the fixing screws, which are ingested by the fan in the tip region. The Fan + Frame configuration (Fig. 13c) is characterized by less coherent vortex

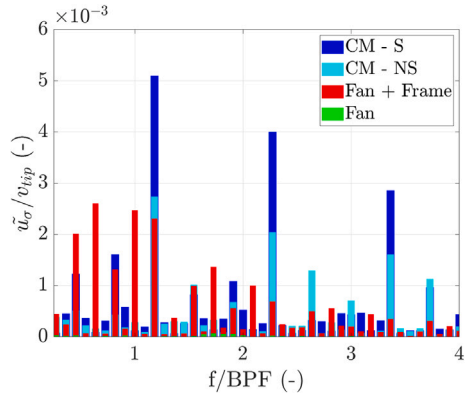

Fig. 14. Azimuthal mode decomposition of the axial velocity component standard deviation sampled on a fully circular line at $r/R_{tip} = 0.9$ in a plane located at $x/D = -0.14$.

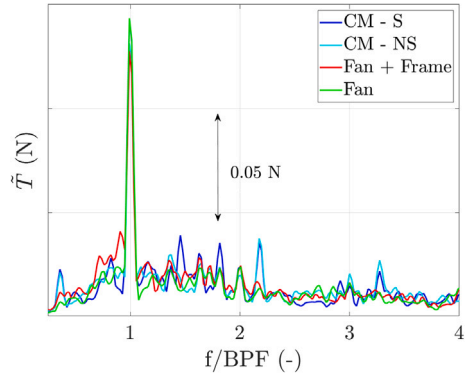

Fig. 15. Spectrum of the thrust given by all the 11 blades.

structures, because of less strong velocity gradients. The vortex structures are due to the flow distortions due to the square-to-round shape transition between the casing and the fan. Finally, the Fan configuration (Fig. 13d) shows vortex structures only in the near tip region wrapping around the rotating ring. They are associated with the tip separation seen in Fig. 12 and with the tip leakage flow that occurs in the tip clearance.

The impact of the different recirculation patterns upstream of the fan is further quantified by looking at the spatial Fourier transform (tilde superscript) of the axial velocity standard deviation u_σ in Fig. 14. The quantities are sampled on a circular line of radius $r/R_{tip} = 0.9$ at $x/D = -0.14$. The frequency f has been made dimensionless with the BPF. The Cooling Module configurations are characterized by prominent humps at $f/BPF = 4/11$ and harmonics. This happens because the vortex structures concentrated at the center of each side of the casing (4) interact with each of the 11 blades. Moreover, contributions at $f/BPF = 8/11$ and harmonics are also seen, being the result of the interaction of the blades with the wake of the 8 cylinders upstream in the casing. When the gaps are present (CM-NS), a smaller amplitude in the peaks is seen, as the recirculation is spread all along the sides of the casing and not concentrated at the center of each side, as shown in Fig. 13. The Fan + Frame configuration is characterized by higher amplitude at f/BPF up to 2, as a consequence of the recirculation taking place in the casing when the porous medium is removed (Fig. 13c). Finally, the Fan configuration shows almost no fluctuations when compared with the other configurations, as there are only a few vortex structures upstream that weakly interact with the blades.

To conclude the aerodynamic analyses, the spectral content of the unsteady thrust $\tilde{T}$ given by the entire fan is shown in Fig. 15. The

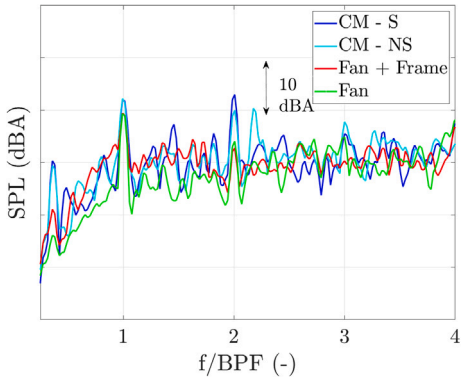

Fig. 16. Pressure fluctuations $2.15D$ along the fan axis upstream.

peak at the BPF is prominent in all the cases, with the Fan configuration showing the highest and the Fan + Frame configuration the lowest value. This behavior has been explained in a previous work [9]. It is the result of the interaction of each blade with a localized low-velocity area in the interstage between the rotor and the stator, which is caused by a honeycomb-like structure that is present for structural purposes. Furthermore, all the configurations show almost unchanged values at higher BPF harmonics except for the CM-NS configuration at $f/BPF = 3$, which exhibits slightly higher fluctuations. At frequencies that are not the BPF and its harmonics, the shape of the thrust spectrum is similar to the velocity azimuthal mode decomposition seen in Fig. 14. The CM configurations are both characterized by several inter-harmonic narrow-band humps which highlight the thrust fluctuations due to the periodic interaction of the blades with the above-seen inflow inhomogeneities, such as the merging vortex structures at the center of each side of the casing and the wake of the 8 cylinders that hold the fixing screws. The CM-S configuration is characterized by more prominent inter-harmonic humps, such as the two at $f/BPF = 1.45$ and $f/BPF = 1.81$. This is due to the 4 localized recirculation spots (Fig. 13). The Fan + Frame configuration is characterized by a higher broadband content for $0.5 \leq f/BPF \leq 1$ due to stronger recirculation in the casing in this configuration. In contrast, the Fan alone case shows almost no inter-harmonic hump except for a slight fluctuation at $f/BPF = 1.81$, which is associated with rotor–stator interaction phenomena, as both the blades and vanes are not equally spaced.

6.2. Acoustic results

Fig. 16 shows the spectrum of the pressure fluctuations sampled at $x/D = -2.15$, $y/D = 0$, and $z/D = 0$, as in the experiments. At the BPF and harmonics, both the CM configurations show higher intensity than the Fan + Frame and Fan configurations. This is associated both with the higher mean loading of these two configurations, as shown in Fig. 11 and with the higher intensity of the fluctuations described in the azimuthal decomposition of the inflow velocity in Fig. 14. Moreover, since these two configurations are simulated in the semi-anechoic room, unlike the Fan + Frame and Fan ones, it can be expected that the recirculation pattern in the room plays a role in the tones at BPF and harmonics prominence, as reported in [9]. Furthermore, the CM configurations are characterized by several inter-harmonic humps at frequencies $f/BPF = 4/11$, $f/BPF = 8/11$, and harmonics, which are given by the interaction between the rotor and the periodic inflow inhomogeneities due to the presence of the square casing and the 8 cylinders that house the screws. The CM-NS configuration shows more prominent peaks at these frequencies, as expected. The broadband content of the Fan + Frame configuration is higher for $f/BPF < 2$, which is attributed to the stronger recirculation pattern in the casing, as seen in Figs. 7 and 14. Moreover, the higher frequency broadband contribution (approximately

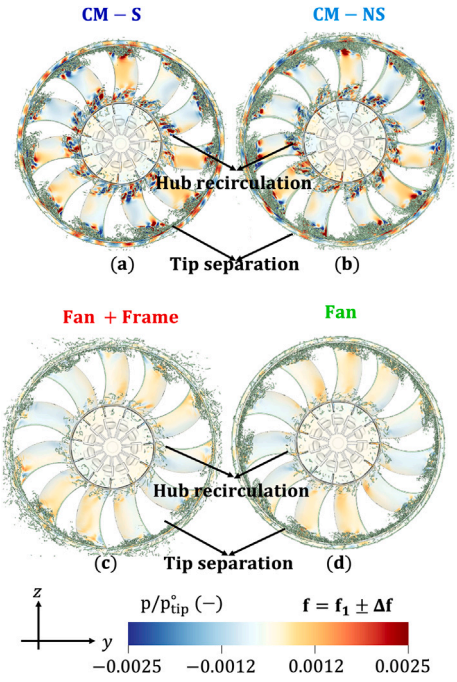

Fig. 17. Band-pass filtered wall pressure fluctuations around $f_1/BPF = 1.2$ with a bandwidth $\Delta f/BPF = 0.18$ and instantaneous $\Lambda_2 = -2.5 \cdot 10^7$ 1/s isosurfaces (rear view). (a): CM-S. (b): CM-NS. (c): Fan + Frame. (d): Fan.

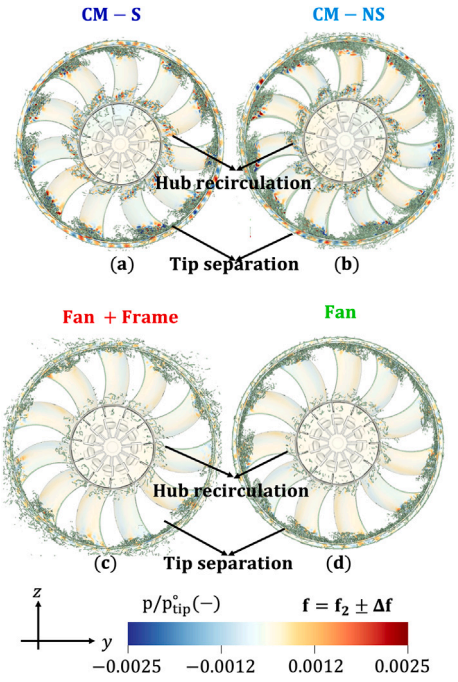

Fig. 18. Band-pass filtered wall pressure fluctuations around $f_2/BPF = 2.6$ with a bandwidth $\Delta f/BPF = 0.18$ and instantaneous $\Lambda_2 = -2.5 \cdot 10^7$ 1/s isosurfaces (rear view). (a): CM-S. (b): CM-NS. (c): Fan + Frame. (d): Fan.

for $f/BPF > 2$) shows almost the same levels for all four simulated configurations. This suggests that these frequencies are dominated by a common physical mechanism such as trailing edge noise. Finally, it can be noted that some inter-harmonic frequencies show humps, but they cannot be associated with the effect of the flow recirculation on the 4 casing sides or with the effect of the wake shed by the 8 cylinders, i.e., multiples of $f/BPF = 4/11$ or $f/BPF = 8/11$. For instance, three inter-harmonic frequency regions, i.e., $f_1/BPF = 1.2$, $f_2/BPF = 2.6$, and $f_3/BPF = 3.8$ are identified as worth of additional investigation.

The band-pass filtered wall pressure p is shown in Figs. 17–19 centered respectively at f_1, f_2, and f_3 with a bandwidth $\Delta f/BPF = 0.18$. The pressure has been made dimensionless with the tip dynamic pressure $p^\circ_{tip} = \frac{1}{2}\rho v^2_{tip}$. On top of the surface plots, the isosurfaces of instantaneous $\Lambda_2 = -2.5 \cdot 10^7$ 1/s are shown. From a quick visual inspection of all three figures is clear that the main wall pressure peaks are located where the vortex structures, identified through the Λ_2 isosurfaces, are. At $f_1/BPF = 1.2$ (Fig. 17) it can be noted that both the CM configurations (Fig. 17a and b) are characterized by higher amplitude, mainly located at the hub and in the near tip region, between the blade tip and the rotating ring. The former is associated with the presence of secondary recirculation at the hub, as shown in Fig. 8, while the latter is associated with both the tip separation seen in Fig. 12 and with the higher inflow gradients seen in Fig. 10. The peaks, moreover, seem to expand over the whole blade span since the wavelength $\lambda_1 = \frac{c_0}{f_1} = 1.1D$, where c_0 is the speed of sound, is greater than the fan diameter. The Fan + Frame and Fan configurations (Fig. 17c) are then characterized by less intense amplitude both at the hub and tip, albeit the Fan configuration shows more structures at the tip, due to the stronger separation seen in Fig. 12. A similar pattern in the amplitude is seen at $f_2/BPF = 2.6$ (Fig. 18). However, the peaks are now located only at the tip while in the CM configurations (Fig. 18a and b) at the hub as well. Finally, at $f_3/BPF = 3.8$ (Fig. 19), it can be noted that the hub peaks in the CM configurations (Fig. 19a and b) are less intense, while the fluctuations at the tip maintain almost the same levels as in the previous figure. It can be concluded that the inter-harmonic humps at frequencies that are not

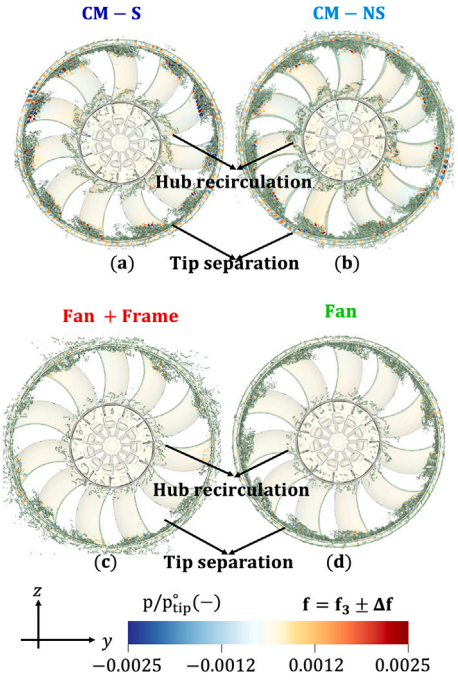

Fig. 19. Band-pass filtered wall pressure fluctuations around $f_3/BPF = 3.8$ with a bandwidth $\Delta f/BPF = 0.18$ and instantaneous $\Lambda_2 = -2.5 \cdot 10^7$ 1/s isosurfaces (rear view). (a): CM-S. (b): CM-NS. (c): Fan + Frame. (d): Fan.

harmonics of $f/BPF = 4/11$ are given by the hub and tip separation vortices, which are stronger in the CM configurations, due to the presence of higher pressure (i.e., velocity) gradients because of the porous medium.

The directivity patterns at the BPF and its first two harmonics, as well as on the overall SPL in the frequency range $0 \leq f/BPF \leq 4$, are

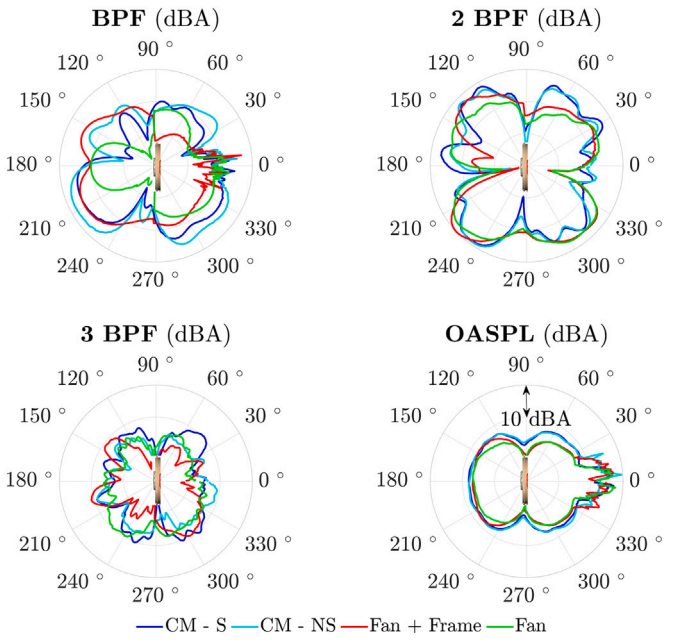

Fig. 20. Directivity plots of the pressure fluctuations at the BPF, the first two harmonics of the BPF, and the OASPL over the frequency range $0 \leq f/BPF \leq 4$.

shown in Fig. 20. The plot shows the SPL on a full circular array of 360 probes located at $z/D = 0$. At the BPF, it can be seen that both the porous medium and the frame are seen to highly influence the directivity, both increasing the maximum levels and shifting the maximum from 180° to about 210°. These important differences are associated with both the higher blade loading harmonics near the BPF and possible acoustic reflections of the heat exchanger and the semi-anechoic room floor. This is consistent with Moreau et al. [42], which highlighted the generation of more lobes on the directivity patterns due to the acoustic scattering of the floor. Moreover, the CM-NS configuration shows higher contributions in the range between 150° and 90° with respect to the CM-S configuration. This is due to the higher radiation efficiency of the CM-NS configuration, since the higher recirculation in the casing results in an increase of blade loading fluctuations near the BPF, as seen in Fig. 15. At the first two BPF harmonics, instead, the differences are less evident, and the OASPL shows almost no differences between all the simulated configurations. In addition, all four configurations show a strongly varying pattern around 0° at the BPF, which is related to the presence of the wake periodically shed by the fan. This can be observed also in the OASPL plot, which shows a similar pattern around 0°.

7. Conclusions

The results presented in this study offer a detailed examination of the aerodynamic and acoustic effects of key installation features in a complete automotive engine cooling module. Three different configurations are analyzed through numerical simulations at free-blowing conditions, including the full cooling module, the module without the porous medium but with the solid frame, and the fan alone. The latter two configurations have the same global pressure rise caused by the porous medium in the first configuration. The full cooling module configuration includes two different types of installations, where the axial gap between the heat exchanger and its casing is both sealed and not sealed. Each of these factors plays a distinct role in modifying the fan performance and noise generation, particularly through their influence on upstream aerodynamics.

The presence or absence of small axial gaps between the heat exchanger and the casing has little effect on the mean aerodynamic performance of the fan. On the other hand, the more spread recirculation pattern in the casing upstream of the fan results in less prominent inter-harmonic humps in the blade loading harmonics, which, in turn, results in less prominent peaks in the far-field acoustics. The directivity at the BPF is influenced by the gaps, suggesting its importance in the acoustic emission of the module, in contrast to their negligible effects on the fan aerodynamic performance. Therefore, manufacturers shall consider the presence of small axial gaps in the heat exchanger assembly as a potential strategy to mitigate inter-harmonic humps in the far-field noise.

Removing the porous medium while maintaining the same pressure drop across the system results in a decrease in thrust and torque. Moreover, the porous medium focuses the pressure rise on the fan disk. Therefore, without the porous medium, pressure rise becomes more uniformly distributed across the system, affecting the distribution of aerodynamic loading along the blade and, thus, the tonal noise of the fan at the BPF and harmonics. This highlights the importance of accounting not only for the global pressure rise but also for its spatial distribution when selecting and integrating heat exchangers. The increase in inhomogeneity in the upstream flow, when the porous medium is removed, amplifies the noise generated by interactions between the blades and the inflow distortions, particularly in the low-frequency broadband range. Smoother casing transitions and streamlined casing features can provide significant acoustic benefits and should be considered when designing the cooling module.

Finally, it is found that coherent tip vortices are present in all the simulated configurations. They are associated with flow separation occurring in the tip region due to the high inflow velocity to which the fan is subjected. This results in the dominance of tip noise in all the investigated cases. For this reason, strategies aimed at mitigating tip leakage, such as optimized tip clearance or blade sweep, shall be a priority irrespective of the specific installation configuration.

CRediT authorship contribution statement

Francesco Bellelli: Writing – original draft, Visualization, Validation, Investigation, Formal analysis, Data curation, Conceptualization. **Renzo Arina:** Writing – review & editing, Supervision, Resources. **Stéphane Moreau:** Writing – review & editing, Supervision, Resources. **Francesco Avallone:** Writing – review & editing, Supervision, Resources.

Declaration of competing interest

The authors declare that they have no known competing financial interests or personal relationships that could have appeared to influence the work reported in this paper.

Data availability

The data that has been used is confidential.

References

[1] Moreau S, Roger M. Turbomachinery noise review. Int J Turbomach Propuls Power 2024;9:9010011. https://doi.org/10.3390/ijtpp9010011
[2] Amoiridis O, Zarri A, Zamponi R, Pasco Y, Yakhina G, Christophe J, et al. Sound localization and quantification analysis of an automotive engine cooling module. J Sound Vib 2022;517:116534. https://doi.org/10.1016/j.jsv.2021.116534
[3] Piwowarski M, Jakowski D. Areas of Fan Research—A Review of the Literature in Terms of Improving Operating Efficiency and Reducing Noise Emissions. Energies 2023;16(3):10–42. https://doi.org/10.3390/en16031042
[4] Zhou W, Zhou P, Xiang C, Wang Y, Mou J, Cui J. A review of bionic structures in control of aerodynamic noise of centrifugal fans. Energies 2023;16(11):4331. https://doi.org/10.3390/en16114331
[5] Longhouse RE. Noise mechanism separation and design considerations for low tip-speed, axial-flow fans. J Sound Vib 1976;48(4):461–74. https://doi.org/10.1016/0022-460X(76)90550-2
[6] Brooks TF, Pope DS, Marcolini MA. Airfoil self-noise and prediction, Tech. rep., NASA; 1989.
[7] Lallier-Daniels D, Piellard M, Coutty B, Moreau S. Aeroacoustic study of an axial engine cooling module using lattice-Boltzmann simulations and the Ffowcs

Williams and Hawkings' analogy. Eur J Mech - B/Flu 2017;61:244–54. https://doi.org/10.1016/j.euromechflu.2016.10.008
[8] Tyler JM, Sofrin TG. Axial Flow Compressor Noise Studies. In: SAE Technical Paper 620532; 1962. https://doi.org/10.4271/620532
[9] Bellelli F, Arina R, Avallone F. On the impact of operating condition and testing environment on the noise sources in an industrial engine cooling fan. Appl Acoust 2025;227:110–252. https://doi.org/10.1016/j.apacoust.2024.110252
[10] Sharland IJ. Sources of noise in axial flow fans. J Sound Vib 1964;1(3):302–22. https://doi.org/10.1016/0022-460X(64)90068-9
[11] Moreau S, Roger M. Competing broadband noise mechanisms in low-speed axial fans. AIAA J 2007;45(1):48–57. https://doi.org/10.2514/1.14583
[12] Magne S, Moreau S, Berry A. Subharmonic tonal noise from backflow vortices radiated by a low-speed ring fan in uniform inlet flow. J Acoust Soc Am 2015;137(1):228–37. https://doi.org/10.1121/1.4904489
[13] Sortor M. On-system engine cooling fan measurement as a tool for optimizing cooling system airflow performance and noise. SAE Int J Mater Manufacturing 2011;4(1):1221–30. https://doi.org/10.4271/2011-01-1169
[14] Czwielong F, Soldat J, Becker S. On the interactions of the induced flow field of heat exchangers with axial fans. Exp Therm Fluid Sci 2022;139:110697. https://doi.org/10.1016/j.expthermflusci.2022.110697
[15] Zarri A, Botana MB, Christophe J, Schram C. Aerodynamic investigation of the turbulent flow past a louvered-fin-and-tube automotive heat exchanger. Exp Therm Fluid Sci 2024;155:111182. https://doi.org/10.1016/j.expthermflusci.2024.111182
[16] Piellard M, Coutty BB, Le Goff V, Vidal V, Perot F. Direct aeroacoustics simulation of automotive engine cooling fan system: effect of upstream geometry on broadband noise. In: 20th AIAA/CEAS Aeroacoustics Conference; 2014. https://doi.org/10.2514/6.2014-2455
[17] Zhang PF, Zhu MT, Li ZJ, Wang K. The cooling module aerodynamic noise prediction considering porous media. Appl Mech Mater 2014;711:20–6. https://doi.org/10.4028/www.scientific.net/AMM.711.20.
[18] Tebib S, Jayasimha AB, Moreau S, Demory B, Henner M, Mann A, et al. Detailed noise analysis of automotive engine cooling modules using the Lattice-Boltzmann Method. In: AIAA AVIATION 2023 Forum; 2023. https://doi.org/10.2514/6.2023-3205
[19] Czwielong F, Krömer F, Becker S. Experimental investigations of the sound emission of axial fans under the influence of suction-side heat exchangers. In: 25th AIAA/CEAS Aeroacoustics Conference; 2019. https://doi.org/10.2514/6.2019-2618
[20] Bellelli F, Arina R, Moreau S, Avallone F. Aeroacoustics analysis of radiator installation effects in a pulling engine cooling module. In: FAN 2025; 2025.
[21] He X, Luo L-S. Theory of the lattice boltzmann method: From the boltzmann equation to the lattice boltzmann equation. Phys Rev E Stat Phys Plasmas Fluids Relat Interdiscip Topics 1997;56(6):6811–7. https://doi.org/10.1103/PhysRevE.56.6811
[22] Sharma KV, Straka R, Tavares FW. Current status of lattice boltzmann methods applied to aerodynamic, aeroacoustic, and thermal flows. Prog Aerosp Sci 2020;115:100616. https://doi.org/10.1016/j.paerosci.2020.100616
[23] Shao W, Li J. Review of Lattice Boltzmann method applied to computational aeroacoustics. Arch Acoust 2023;44:215–38. https://doi.org/10.24425/aoa.2019.128486
[24] Ghodake D, Sanjosé M, Moreau S, Henner M. Effect of sweep on Axial Fan Noise Sources Using the Lattice Boltzmann method. Int J Turbomach Propuls Power 2022;7(4):34. https://doi.org/10.3390/ijtpp7040034
[25] Perot F, Moreau S, Kim M-S, Henner M, Neal D. Direct aeroacoustics predictions of a low speed axial fan. In: 16th AIAA/CEAS Aeroacoustics Conference; 2010. https://doi.org/10.2514/6.2010-3887
[26] Antoniou E, Romani G, Jantzen A, Czwielong F, Schoder S. Numerical flow noise simulation of an axial fan with a lattice-boltzmann solver. Acta Acust 2023;7:2023060. https://doi.org/10.1051/aacus/2023060
[27] Bhatnagar PL, Gross EP, Krook M. A model for collision processes in gases. i. small amplitude processes in charged and neutral one-component systems. Phys Rev 1954;94(3):511–25. https://doi.org/10.1103/PhysRev.94.511
[28] Chapman S, Cowling TG. The mathematical theory of non-uniform gases: An account of the kinetic theory of viscosity, thermal conduction and diffusion in gases. Cambridge: Cambridge University Press; 1991.
[29] Qian YH, D'Humières D, Lallemand P. Lattice BGK models for navier-stokes equation. EPL 1992;17(6):479–84. https://doi.org/10.1209/0295-5075/17/6/001
[30] Zhang R, Sun C, Li Y, Satti R, Shock R, Hoch J, et al. Lattice boltzmann approach for local reference frames. Commun Comput Phys 2011;9(5):1193–205. https://doi.org/10.4208/cicp.021109.111110s
[31] Chen H, Kandasamy S, Orszag S, Shock R, Succi S, Yakhot V. Extended boltzmann kinetic equation for turbulent flows. Sci. 2003;301(5633):633–6. https://doi.org/10.1126/science.1085048
[32] Teixeira CM. Incorporating turbulence models into the Lattice-Boltzmann method. Int J Mod Phys C 1998;9(08):1159–75. https://doi.org/10.1142/S0129183198001060
[33] Launder BE, Spalding DB. The numerical computation of turbulent flows. Comput Methods Appl Mech Eng 1974;3(2):269–89. https://doi.org/10.1016/B978-0-08-030937-8.50016-7
[34] Welch P. The use of fast fourier transform for the estimation of power spectra: A method based on time averaging over short, modified periodograms. IEEE Trans Audio Electroacoust 1967;15(2):70–3. https://doi.org/10.1109/TAU.1967.1161901
[35] Avallone F, Ragni D, Casalino D. On the effect of the tip-clearance ratio on the aeroacoustics of a diffuser-augmented wind turbine. Renew Energy 2020;152:1317–27. https://doi.org/10.1016/j.renene.2020.01.064
[36] Whitaker S. Flow in porous media i: A theoretical derivation of darcy's law. Transp in porous media 1986;1:3–25. https://doi.org/10.1007/bf01036523
[37] Richardson LF. The approximate arithmetical solution by finite differences of physical problems involving differential equations, with an application to the stresses in a masonry dam. Philos Trans R Soc Lond 1911;210(459–470):307–57. https://doi.org/10.1098/rsta.1911.0009
[38] Avallone F, Van Der Velden WCP, Ragni D, Casalino D. Noise reduction mechanisms of sawtooth and combed-sawtooth trailing-edge serrations. J Fluid Mech 2018;848:560–91. https://doi.org/10.1017/jfm.2018.377
[39] Moreau S, Sanjose M. Sub-harmonic broadband humps and tip noise in low-speed ring fans. J Acoust Soc Am 2016;139(1):118–27. https://doi.org/10.1121/1.4939493
[40] Teruna C, Rego L, Casalino D, Ragni D, Avallone F. A numerical study on aircraft noise mitigation using porous stator concepts. Aerosp. 2022;9(2):9020070. https://doi.org/10.3390/aerospace9020070
[41] Roache PJ. Perspective: a method for uniform reporting of grid refinement studies. J Fluids Eng 1994:405–13. https://doi.org/10.1115/1.2910291
[42] Moreau S. Direct noise computation of low-speed ring fans. Acta Acust united with Acust 2019;105(1):30–42. https://doi.org/10.3813/aaa.919285